Organic light-emitting transistors with an efficiency that outperforms the equivalent light-emitting diodes

Raffaella Capelli[1]*, Stefano Toffanin[1], Gianluca Generali[1], Hakan Usta[2], Antonio Facchetti[2] and Michele Muccini[1,3]*

The potential of organic semiconductor-based devices for light generation is demonstrated by the commercialization of display technologies based on organic light-emitting diodes (OLEDs). Nonetheless, exciton quenching and photon loss processes still limit OLED efficiency and brightness. Organic light-emitting transistors (OLETs) are alternative light sources combining, in the same architecture, the switching mechanism of a thin-film transistor and an electroluminescent device. Thus, OLETs could open a new era in organic optoelectronics and serve as testbeds to address general fundamental optoelectronic and photonic issues. Here, we introduce the concept of using a p-channel/emitter/n-channel trilayer semiconducting heterostructure in OLETs, providing a new approach to markedly improve OLET performance and address these open questions. In this architecture, exciton–charge annihilation and electrode photon losses are prevented. Our devices are >100 times more efficient than the equivalent OLED, >2× more efficient than the optimized OLED with the same emitting layer and >10 times more efficient than any other reported OLETs.

Organic semiconductor-based devices such as OLEDs, solar cells, memories and field-effect transistors (OFETs) are predicted to reduce fabrication costs and enable new functions[1–6]. The OLET (Fig. 1) is another optoelectronic device having the structure of a thin-film transistor and the capability of light generation[7]. Bright/multicolour OLETs may allow electroluminescent display fabrication with simpler driving circuits. Furthermore, the most advanced OLETs possess a huge technological potential for the realization of intense nanoscale light sources and highly integrated optoelectronic systems, including the long-researched electrically pumped organic laser[8–16]. In terms of performance and reliability, OLED technology is by far the most developed, and active matrix OLED displays have been introduced into the market. However, detrimental device-related processes affecting OLED operation under high-injection conditions are the exciton–charge interactions and the photon losses at the electrodes. The proximity (within tens of nanometres) of the contacts to the OLED light-generation region induces losses owing to the absorption of the emitted photons. Moreover, the highly dense electron and hole currents converge to the light-emitting layer, where they form, but spatially coexist with the excitons, and lead to significant exciton–charge quenching[17–20]. Indeed, this mechanism is predicted to be greater than any other quenching effects[21] and should be controlled to enhance the OLED efficiency, brightness and stability even further. Thus, the focus of OLET development is the possibility to enable new display/light source technologies, and exploit a transport geometry to suppress the deleterious photon losses and exciton quenching mechanisms inherent in the OLED architecture. So far, only the exciton–metal interaction has been successfully addressed in OLETs based on ambipolar single layers[22–27]. Under proper bias conditions, the spatial location of the light-emitting area is far from the metal electrodes, preventing exciton–metal quenching. However, in these single-layer devices the charge carrier accumulation and the exciton formation zones largely coincide, leading to severe exciton–charge quenching. Indeed, even in the most impressive demonstration so far, the external quantum efficiency (EQE) does not exceed 0.5–0.6% (ref. 28). Consistently, single-layer unipolar OLETs, in which only one type of charge carrier is effectively transported across the channel, reached remarkable results in terms of brightness[29,30], but their EQE is only 0.2%, mainly because excitons are subjected to both metal and charge quenching, and electrode-induced photon losses[29]. A horizontal p–n-heterojunction OLET has also been reported, in which light emission is confined far from the contacts; however, exciton–charge quenching is not avoided[31]. A bilayer approach has been used to improve OLET brightness, or achieve higher and more balanced charge transport. In the first case a highly efficient luminescent layer is superimposed over a unipolar conducting layer[32], whereas in the second case p-type and n-type transport films are directly in contact with each other[33]. However, in both cases this device architecture does not offer any control of the exciton quenching and photon losses, as the light-emitting area is in contact with the minority carrier injection electrode. Excitons interact with accumulated charges and the metal electrode, whereas photons are absorbed by the contacts. In this work, we report the first trilayer heterostructure approach for OLETs enabling simultaneous control of electrode-induced photon losses, and exciton–metal and exciton–charge interactions. OLET devices with EQEs of 5% are demonstrated, which exceeds the best OLEDs based on the same emitting layer and optimized transport layers (2.2%; ref. 34).

The trilayer heterostructure OLETs used in this study (Fig. 1a) were fabricated on glass/indium tin oxide (ITO; gate contact,

[1]Consiglio Nazionale delle Ricerche (CNR), Istituto per lo Studio dei Materiali Nanostrutturati (ISMN), via P. Gobetti 101, I-40129 Bologna, Italy, [2]Polyera Corporation, 8045 Lamon Avenue, Skokie, Illinois 60077, USA, [3]E.T.C. srl, via P. Gobetti 101, I-40129 Bologna, Italy. *e-mail: r.capelli@bo.ismn.cnr.it; m.muccini@bo.ismn.cnr.it.
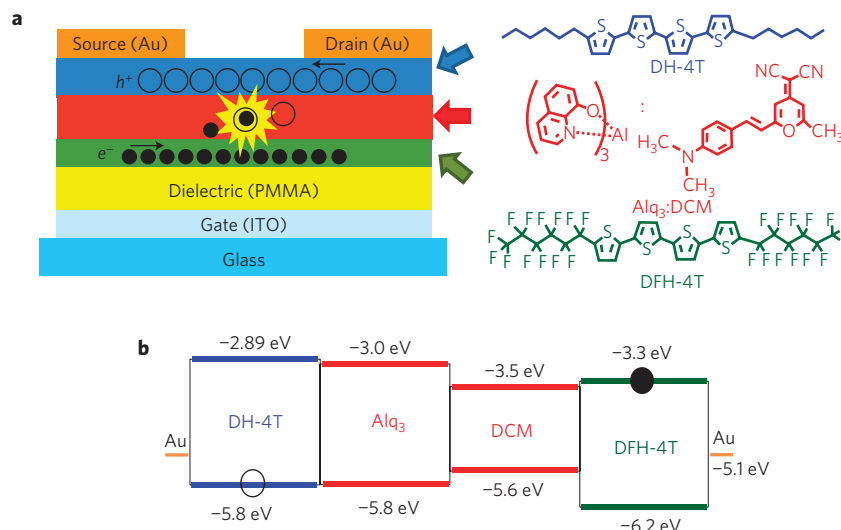
Figure 1 | Trilayer OLET device structure and active materials forming the heterostructure. a, Schematic representation of the trilayer OLET device with the chemical structure of each material making up the device active region. The field-effect charge transport and the light-generation processes are also sketched. **b**, Energy-level diagram of the trilayer heterostructure. The energy values of the HOMO and LUMO levels of each molecular material are indicated together with the Fermi level of the gold contacts.

150 nm)/PMMA (dielectric, 450 nm) substrates. The active region consists of the superposition of three organic layers. The first, in contact with the PMMA dielectric, and the third layers are field-effect electron-transporting (n-type, 7 nm) and hole-transporting (p-type, 15 nm) semiconductors, respectively, whereas the middle layer is a light-emitting host–guest matrix (40 nm). The device structure is completed by the deposition of the gold (source and drain, 50 nm) contacts. To enable the vertical charge diffusion process, the basis of the OLET electroluminescence mechanism, energetic compatibility between the materials forming the heterostructure is required. The lowest unoccupied molecular orbital (LUMO) of the n-type transport layer should be equal to or higher than the LUMO of the guest matrix in the central layer, whereas the highest occupied molecular orbital (HOMO) of the p-type transport layer should be equal to or lower than the guest matrix HOMO level. Furthermore, the morphology of these films must allow the formation of a continuous multistack. Meeting these requirements is not trivial and, after several attempts, we identified the α, ω-disubstituted-quaterthiophenes with hexyl (DH-4T, Polyera ActivInk P0400) and perfluorohexyl (DFH-4T, Polyera ActivInk N0700) chains as the hole and the electron transporting films, respectively[35]. To realize the central light-formation layer a blend of host *tris*(8-hydroxyquinolinato)aluminium (Alq$_3$) and guest 4-(dicyanomethylene)-2-methyl-6-(p-dimethylaminostyryl)-4H-pyran (DCM) was used. Figure 1 also shows the chemical structure and the electrochemically derived energy-level diagram of the organic heterostructure, clearly showing the energetic compatibility of these materials.

As part of the preliminary study, single-layer OFETs based on DFH-4T and DH-4T on glass/ITO/PMMA substrates (Au contacts) were fabricated. They exhibited electron and hole mobilities of 0.5 cm^2 V^{-1} s^{-1} and 0.08 cm^2 V^{-1} s^{-1}, respectively, 2–5 times larger than those reported on the Si/SiO$_2$ and Al/PMMA substrates[35,36]. Atomic force microscopy (AFM) of the films on Si/SiO$_2$ substrates evidenced a bidimensional layer-by-layer film growth, resulting in uniform and flat surface morphologies[35,37–40]. Importantly, confocal laser scanning microscopy images (CLSM, see Supplementary Fig. S2) indicate that similar flat surface morphologies are obtained on glass/ITO/PMMA substrates although the DH-4T domains are significantly larger than those of DFH-4T. This

condition is essential for the realization of our multilayer OLETs (see below). DFH-4T/DH-4T bilayer OFETs were also fabricated (Supplementary Fig. S3a) to evaluate the charge transport properties of these bilayer heterostructures. The FET characteristics (Supplementary Fig. S3b,c) demonstrate an ambipolar behaviour with a state-of-the-art balanced hole (0.01 cm^2 V^{-1} s^{-1}, V_T^P = +40 V) and electron (0.01 cm^2 V^{-1} s^{-1}, V_T^N = −40 V) transport and no hysteresis[33,41–43]. Importantly, no light emission was collected from these bilayer devices. The good electrical properties of these oligothiophene FETs, coupled with the possibility to control the growth morphology, make them good candidates for trilayer heterostructure OLET fabrication.

Figure 2 shows an optical image of a lit trilayer OLET ($L = 150\,\mu$m and $W = 20$ cm) as well as a zoom of the OLET channel with the light generated within it. Differently from the bilayer FET, the trilayer OLET generates light when switched on. In Fig. 2c, the OLET photoluminescence and electroluminescence spectra are compared. The central emission peak is positioned at 600 nm in both cases and corresponds to the DCM emission. In the electroluminescence spectrum a shoulder appears at about 530 nm that can be attributed to the residual Alq$_3$ emission[44].

The OLET optoelectronic characteristics are reported in Fig. 3. The curves shown in Fig. 3a and b were obtained by operating the device within the unipolar regime ($|V_{DS}| = |V_{GS}|$) and correspond to the field-effect transport of only electrons and holes, respectively. Thus, Fig. 3a shows the charge transport taking place in the DFH-4T layer and Fig. 3b shows the charge transport occurring in the DH-4T film. Light emission is collected in correspondence of the electron transport (Fig. 3a). When charge carriers recombine at the drain electrode through one, or more, upper layers, a diode-like mechanism gives rise to light emission[32,33]. This process is characterized by a linear correlation between the electroluminescence and current intensity, clearly observable in Fig. 3a, and by the spatial localization of the emission region at the drain electrode region. A large difference between the hole and the electron currents is observed in this OFET structure. Although the electron mobilities are comparable to those of the single-layer DFH-4T OFETs (0.5 cm^2 V^{-1} s^{-1}, V_T^N = +34 V, Supplementary Fig. S1), the hole mobilities are severely degraded with respect to the DH-4T OFETs (5 × 10^{-5} cm^2 V^{-1} s^{-1}, V_T^P = −40 V). Thus, the insertion of the third Alq$_3$:DCM layer between the DFH-4T and
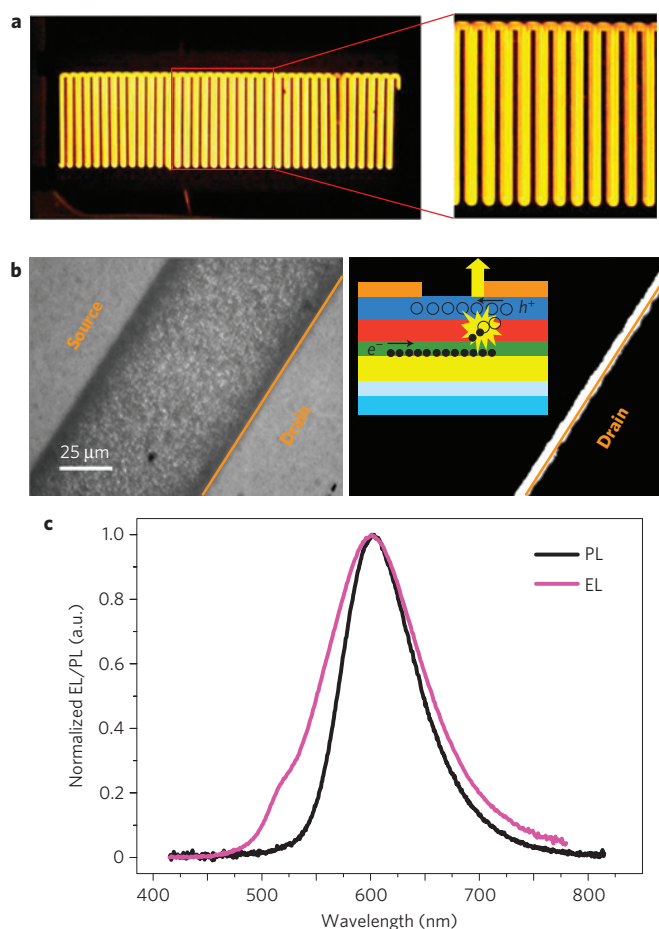
497

Figure 2 | Optical micrographs of the lit trilayer OLET and its emission spectra. a, Optical micrograph of the interdigitated trilayer heterostructure OLET biased with $V_{DS} = V_{GS} = 90$ V. Channel length and channel width are 150 µm and 20 cm, respectively. **b**, Optical micrograph of the OLET channel when no bias is applied to the device, and when the applied bias is $V_{DS} = V_{GS} = 90$ V. The schematic representation of the trilayer heterostructure OLET showing the expected location of the light-generation area is reported in the inset. **c**, Comparison between the electroluminescence (EL) and photoluminescence (PL) spectra of the trilayer heterostructure OLET.

the DH-4T films strongly affects the transport properties of the top DH-4T layer.

AFM images carried out on each layer of the heterostructure (Fig. 3d–f) account for the degraded hole transport in these OLETs. Figure 3e shows that DFH-4T films vapour-deposited on the PMMA surface form two-dimensional islands which then coalesce completely in the first monolayer. An incipient three-dimensional growth with the formation of thick elongated needles is also present in the 7-nm-thick film. Figure 3f shows the morphology of a 40-nm-thick Alq_3:DCM film grown on the previous DFH-4T layer. The surface of this layer is composed by three-dimensional globular aggregates with 100–300 nm diameters. Clearly the surface roughness and the presence of voids and protuberances partially prevent the layer-by-layer growth of the 20-nm-thick DH-4T film on the optical layer (Fig. 3f). The DH-4T film topology mirrors that of the underlying Alq_3:DCM layer, resulting in an inhomogeneous and poorly connected film that limits transport efficiency[45].

When the device bias conditions allow simultaneous charge injection from both the source and drain electrodes ($|V_{GS}| < |V_{DS}|$) the OLET is in the ambipolar operation regime, representative transfer curves of which are reported in Fig. 3c (linear scale). The

strong unbalanced transport in the DFH-4T/Alq3:DCM/DH-4T heterostructures hinders the 'V' shape characteristic of ambipolar transistors operated in transfer mode. Consequently, the ambipolar (Fig. 3c) and unipolar (Fig. 3a) electrical transfer curves are very similar. However, despite the current similarity, the comparison between Fig. 3a and c clearly shows that a new mechanism of electroluminescence generation is taking place in these OLETs when operated in the ambipolar regime. The shaded area in Fig. 3c highlights the electroluminescence produced by the ambipolar current.

The optical micrographs of the device channel (Fig. 4) show the position of the light-emitting region with respect to the edge of the drain electrode as a function of the applied voltages. The first frame (Fig. 4a) shows the optical image of the reference device channel, where the drain electrode edge is clearly recognizable and marked by a yellow line. It can be observed in Fig. 4b that in the ambipolar operation mode the narrow light-emitting stripe is located far from the drain electrodes, at a distance of ~8 µm. By increasing the gate voltage, the emitting region broadens and shifts towards the drain electrode. Figure 4 therefore confirms that the ambipolar light-formation process takes place well inside the channel, far from the electrodes, thus preventing photon losses at the injection electrodes and the exciton–metal quenching. Moreover, as in the trilayer structure the light-emitting layer is physically separated from the charge flows, exciton–charge quenching is also simultaneously prevented. The light-generation process is based on the charge percolation of electrons and holes moving from the respective transport layers to the Alq_3:DCM layer, where excitons are formed. The transverse electric field generated by electron and hole accumulation in the DFH-4T and DH-4T films, respectively, promotes charge percolation. The nature of the force driving this process, which is correlated to the electron–hole annihilation capability of the central recombination film, leads to a self-regulated equilibrium between the amount of charges located in the transport layers and those entering the optical layer. It is known that in ambipolar OLETs, where the recombination occurs well within the channel, all injected electrons and holes must recombine, because the charges cannot move through several micrometres of an accumulation layer of opposite charge without recombining[23]. In the trilayer OLET this holds true for the charges entering the recombination layer. It is expected that exciton–charge quenching is prevented in the trilayer OLET because: (1) there is no overlap of the opposite charge accumulation layers; (2) the recombination layer has a thickness of 40 nm, which decreases the spatial density of excitons and charges; and (3) excitons do not interact with trapped charges eventually localized at the dielectric interface that are likely to be luminescence quenching sites[28].

A quantitative analysis of the optical properties of the trilayer OLET without considering any exciton–charge quenching (see Supplementary Information) shows that the OLET light outcoupling efficiency is ~27%, which is 30% higher than that of the typical OLED structure (20%). This finding is in agreement with the avoidance of losses at the metal cathode. Any sizable exciton–charge quenching in the trilayer OLET would result in outcoupling efficiencies exceeding 30%, which is unlikely because of the losses at the ITO/PMMA structure. Therefore, the trilayer OLET does not show any sizable exciton–charge quenching and can be regarded as a contactless OLED where exciton–charge quenching is intrinsically prevented. Despite the degraded mobility of the hole minority carriers, the maximum EQE (Fig. 5a) of ambipolar OLETs in this trilayer configuration is higher than 1% and is greater than the maximum EQE estimated for an ideal single-layer OLET (ref. 28). Note that in determining the EQE of the trilayer OLET we did not introduce any corrections related to the device geometry, but calculated the efficiency directly as the ratio between the total
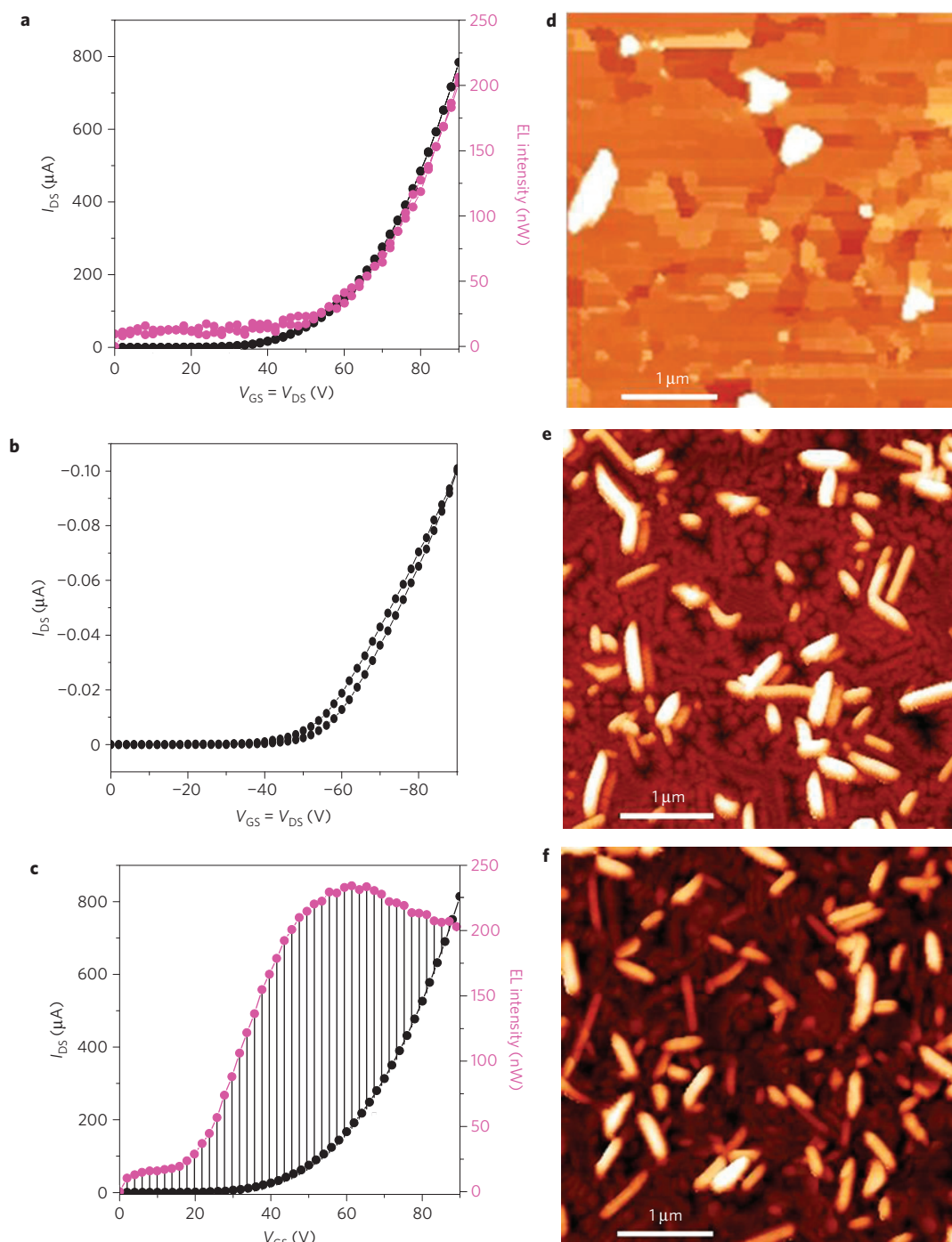
Figure 3 | Optoelectronic characteristics of the trilayer OLET and topographical images of the individual layers forming the heterostructure. a,b, Locus electrical curves of the OLET in n-polarization (**a**) and in p-polarization (**b**). During the n-polarization the electroluminescence output power (magenta) is also collected. **c,** In the transfer characteristic curves, the source–drain current (I_{DS}) is measured keeping the drain–source potential constant at 90 V, while sweeping the gate-source potential from 0 to 90 V. **d,** AFM image of a 7-nm-thick DFH-4T film grown on glass/ITO/PMMA substrate. **e,** AFM image of a 40-nm-thick film of Alq_3:(3%)DCM blend grown on top of the DFH-4T thin film reported in **d**. **f,** AFM image of a 15-nm-thick DH-4T film grown on top of the Alq_3:(3%)DCM film reported in **e**. For ease of comparison the same z-axis colour scale is used for both images **e** and **f**.

emitted photons and the flowing charges (OLET drain current), thereby avoiding any risks of overestimating the EQE.

To verify whether improved interfacial characteristics would increase the efficiency, we fabricated a trilayer OLET with the order of the two charge transport layers reversed. Indeed the flat morphology of the DH-4T layer might be favourable for the realization of a smoother top interface in the heterostructure. The top electrodes were made of LiF/Al to favour electron injection

into the LUMO level of DFH-4T. By implementing the DH-4T thin film (7 nm) as a first layer in contact with the PMMA and the DFH-4T thin film (25 nm) as a top layer, a maximum EQE exceeding 5% and a symmetric EQE profile peaking at the position of maximum ambipolarity (Fig. 5b) is obtained. The impressive improvement of the EQE obtained by controlling the interfaces in the heterostructure demonstrates the potential of our approach. Note that the current density of this reverse device configuration
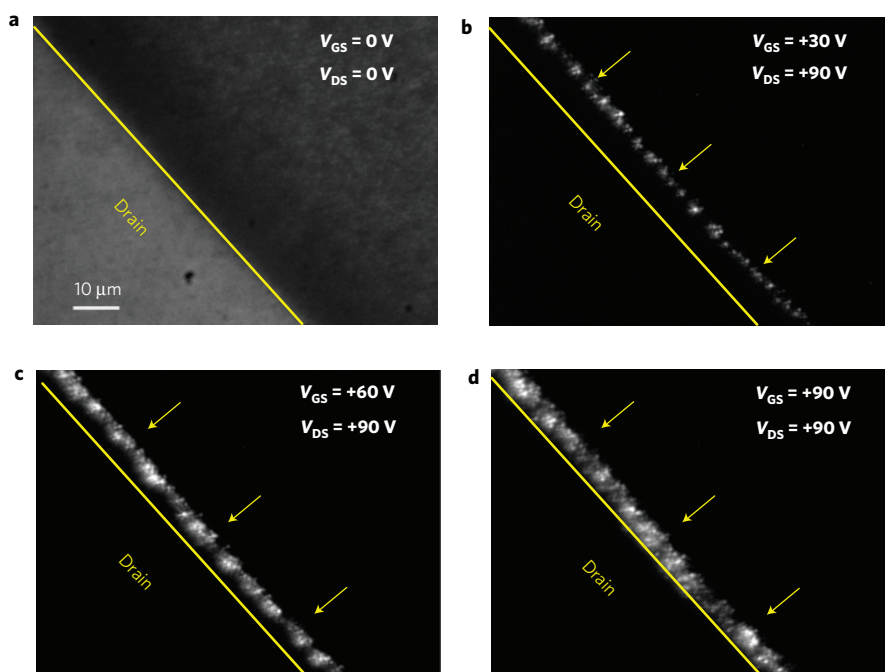
Figure 4 | Images of the light-emitting area within the OLET device channel. a, For reference, an optical micrograph of the device channel without bias, to highlight the position of the drain electrode edge that is marked with a yellow line. **b**–**d**, Optical micrographs of the emission zone within the device channel of the trilayer heterostructure OLET during a transfer scan at $V_{DS} = 90$ V and V_{GS} values of 30 V (**b**), 60 V (**c**) and 90 V (**d**). Three arrows in **b**–**d** indicate the initial position of the recombination and emission zone.
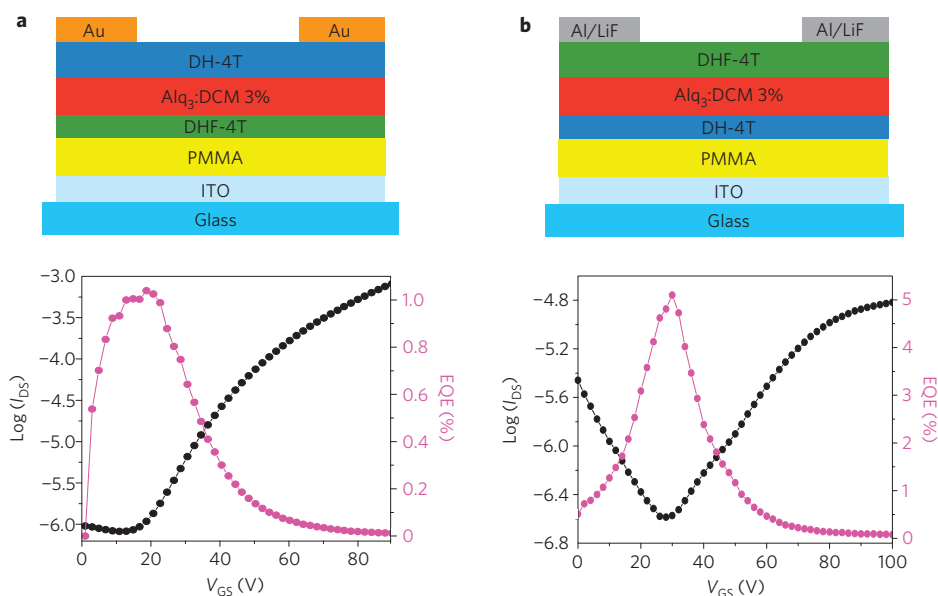

Figure 5 | EQE as a function of the applied gate voltage for the two trilayer heterostructure OLET configurations. a, The bottom layer and the top layer are thin films of DHF-4T and DH-4T, respectively. **b**, The layer configuration of **a** is reversed. The transfer curves with the drain–source current (I_{DS}) plotted on a logarithmic scale are also reported. I_{DS} is measured keeping the drain-source potential constant at 90 V, while sweeping the gate-source potential from 0 to 90 V.

is decreased by a factor of 10 with respect to the previous case, as a result of the large threshold voltage ($>|50|$ V) for both charge types. However, our data demonstrate that the achievement of balanced ambipolar transport in devices with current densities similar to those observed in the first trilayer OLET, would enable OLET devices with simultaneous high efficiency and brightness.

To enable a direct OLED versus OLET experimental comparison we fabricated the device schematized in Fig. 6a, with the aim of implementing the OLET trilayer active region in an equivalent OLED structure. The layer sequence, thickness and film growth parameters are exactly those used for the OLET fabrication and the electrodes are ITO (coated with a poly(3,4-ethylenedioxythiophene) (PEDOT) layer, anode) and Au (cathode). As the workfunctions of ITO/PEDOT and Au are similar, the charge injection conditions in the OLED configuration mimics the OLET case where both the drain and source electrodes are made of gold. The optoelectronic characteristics of this device (Fig. 6b) follow a typical L–I–V OLED behaviour and exhibit a maximum EQE
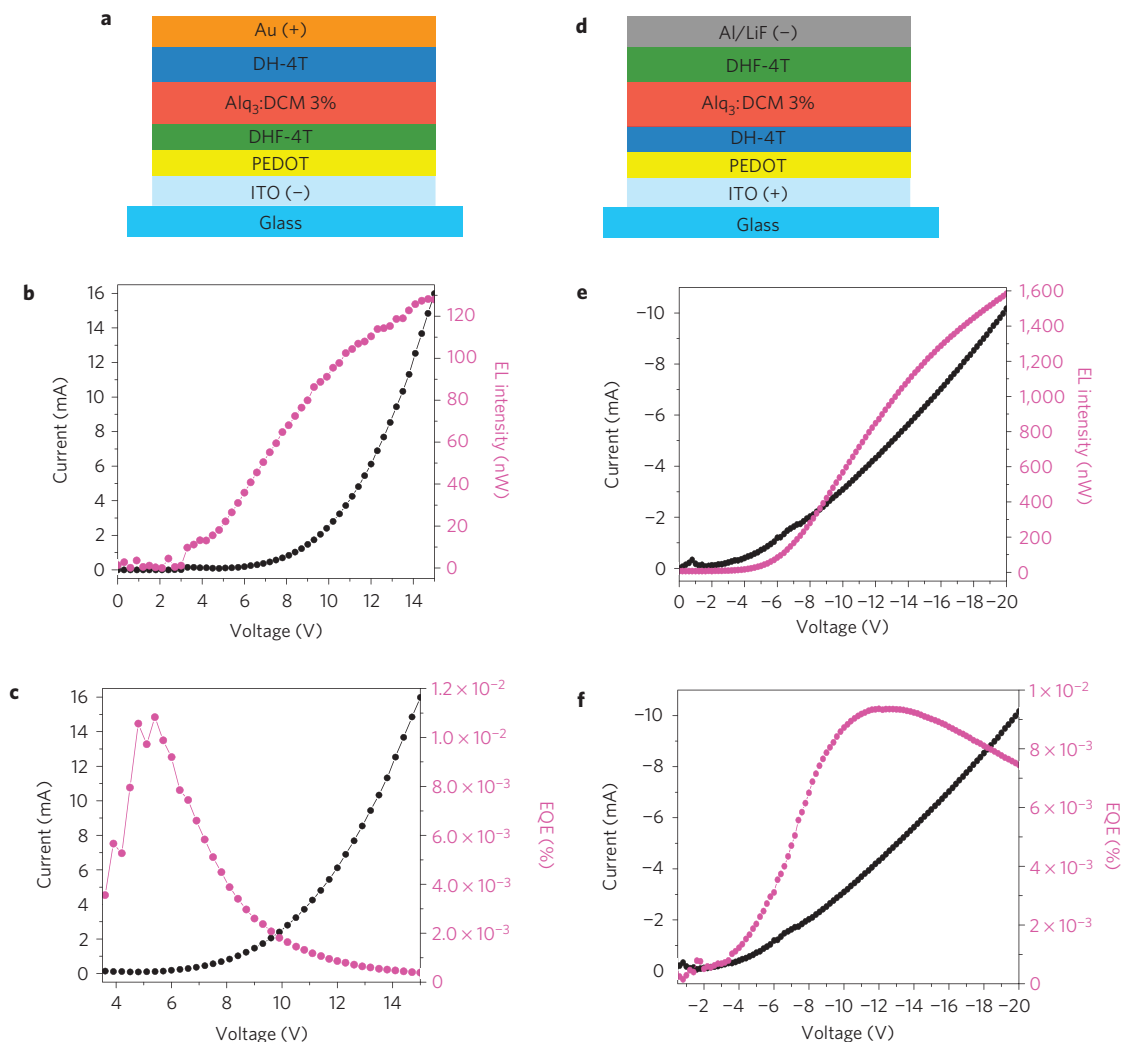
Figure 6 | Device structure and optoelectronic characteristics of the trilayer OLED in direct and reverse configurations. a, Schematic structure of the trilayer OLED in the direct configuration. **b**, Optoelectronic characteristics of the OLED sketched in **a**. **c**, EQE of the direct heterostructure OLED. **d**, Schematic structure of the trilayer OLED in the reverse configuration. **e**, Optoelectronic characteristics of the OLED sketched in **d**. **f**, EQE of the reverse heterostructure OLED.

of ∼0.012% (Fig. 6c). Therefore, the control over the quenching and loss mechanisms results in an organic electroluminescence-generating device with two orders of magnitude higher efficiency.

Furthermore, we fabricated an OLED with the structure ITO/PEDOT/DH-4T/Alq$_3$:DCM/DFH-4T/LiF/Al. In this reverse configuration, hole injection from ITO into the DH-4T hole transport layer, and electron injection from Al into the DFH-4T electron transport layer are optimized. The EQE of this OLED is <0.01% (see Fig. 6f), which is about 500 times lower than that of the corresponding OLET. Finally, the comparison of our OLET with a thoroughly optimized OLED based on Alq$_3$:DCM as the emitting layer[34], provides an important figure of merit to fully appreciate the advantages of the trilayer OLET configuration with respect to conventional OLEDs. Note that the reported EQE of an optimized OLED based on the same emitting layer is 2.2% (ref. 34). All of these data clearly indicate that the quenching and loss processes in our trilayer OLET devices are minimized.

We demonstrated the advantages of using an OLET versus an OLED configuration, and enabled OLETs with the highest efficiency reported so far. The new trilayer heterostructure field-effect concept unravels the full potential of the light-emitting field-effect technology and restricts the limitation of OLEDs to only materials-related issues. Improvements in the top-layer field-effect

mobility at high current density coupled to the use of triplet emitters will enable OLETs with even higher EQE and brightness. In addition to the avoidance of the deleterious exciton–charge quenching and injection-electrode photon losses that we demonstrated in this article, our OLET architecture may also guarantee unprecedented light-extraction efficiencies by using ultrathin layers of ITO or Au as gate electrodes[28]. Moreover, light-outcoupling structures can be easily implemented to extract light from the contact-free top part of the device. The absorption of the generated photons by the charges accumulated within the device is minimized as the thickness of the accumulation layer above the emission layer is only a few nanometres. OLETs also offer an easily processed device architecture that naturally avoids pinholes and shorts between injection contacts, which are among the main technological problems faced by OLEDs.

A critical parameter to be addressed is the device operating voltage. The power efficiency at a given voltage is an essential figure of merit of any light-emitting devices. Present OLETs exhibit their maximum optical power at operating biases of 50–70 V. However, far lower operating voltages could be achieved using high-capacitance gate insulators[46,47]. Indeed, we demonstrated FETs based on the semiconductors used in this study operating at |1–4| V, and their implementation in our OLETs is in progress.

Furthermore, the EQE of our OLETs is maximum for balanced electron and hole currents and is, therefore, achieved in a narrow voltage range. However, despite the technical improvements that are needed, we believe that our trilayer OLETs represent a viable route towards practical organic light-emitting devices with unprecedented performance.

Methods

Device fabrication. Trilayer heterostructure OLETs were fabricated in the top-electrode configuration (see Fig. 1). The substrates consisted of 1 inch square glass coated with a 150-nm-thick layer of ITO that worked as the gate electrode. A 450-nm-thick PMMA film was spin-coated on the substrate in a nitrogen glove box and annealed for 12 h at 120 °C. The films composing the trilayer heterostructure were grown by sublimation in high vacuum, at a base pressure of 5×10^{-7} mbar, in a home-made chamber directly connected to the nitrogen glove box to prevent sample exposure to air during each step of the device realization. For the first OLET configuration the thicknesses of DFH-4T, Alq$_3$:DCM and DH-4T layers were optimized to 7, 40 and 15 nm respectively. The growth rate was fixed at 0.1 Å s^{-1} for both DFH-4T and DH-4T thin films, whereas the Alq$_3$ and DCM molecules were co-sublimed at different growth rates (2 Å s^{-1} for Alq$_3$ and 3 Å min^{-1} for DCM) to guarantee a DCM weight concentration of about 3% in the blend. The Au electrode thickness was 50 nm. For the reversed OLET configuration the thicknesses of the bottom (DH-4T), central (Alq$_3$:DCM) and DFH-4T layers were 7, 40 and 25 nm respectively. The top electrodes were made of LiF/Al (1.2/50 nm). For both configurations the channel length and width were 150 μm and 20 cm, respectively. Devices were encapsulated in the glove box using a glass coverslip and an ultraviolet-cured epoxy sealant. Devices with a channel length of 50 μm were also measured (see Supplementary Fig. S6) and yielded similar EQE values.

Optoelectronic characterization. Optoelectronic characterization of OLETs and OLEDs was carried out using a SUSS probe station, adapted to carry out optoelectronic investigations, coupled to a B1500A Agilent semiconductor device analyser. An S1337 silicon photodiode (Hamamatsu) with a sensitivity of 0.38 A W^{-1} at 600 nm was placed directly in front of the devices and used for simultaneous light-intensity measurements. For the EQE measurements the emitted photons were collected through an Avantes AVA-SPHERE 50-IRR integrating sphere and measured by an Avantes AVA-SPEC 2048 calibrated spectrometer. The EQE was calculated directly as the ratio between the total emitted photons and the charge flow that formed the drain current. Photoluminescence spectra of the trilayer OLET devices were collected in transmission mode by a Hamamatsu multichannel optical analyser (PMA11) after excitation of the device active area with the 375 nm emission of an Oxxius laser diode. Electroluminescence spectra of devices biased using a B1500A Agilent semiconductor device analyser were acquired by a CS200 Konica Minolta spectro-radiometer.

Morphology investigations and optical imaging. CLSM images of the single-layer device channel were carried out with a Nikon Eclipse 2000-E laser scanning confocal microscope. The CLSM images were obtained by exciting the sample with the 485 nm emission line of an Ar$^+$ laser and collecting the photoluminescence emission through the glass substrate with a ×60 magnification objective with 0.7 numerical aperture. Optical micrographs of the OLET device channel and recombination region were taken with the same Nikon Eclipse 2000-E microscope, using a sample holder equipped with electrical connections that placed the optoelectronic device in the focal plane of the microscope. Optical detection was achieved using ×60 or ×90 magnification objectives and a Hamamatsu high-resolution digital camera. AFM topographical images were collected using an NT-MDT Solver Scanning Probe Microscope in the tapping mode with the samples kept in air.

References

1. Yan, H. *et al.* A high-mobility electron-transporting polymer for printed transistors. *Nature* **457,** 680–687 (2009).
2. Forrest, S. R. The path to ubiquitous and low-cost organic electronic appliances on plastic. *Nature* **428,** 911–918 (2004).
3. Malliaras, G. & Friend, R. H. An organic electronics primer. *Phys. Today* **58,** 53–58 (2005).
4. Park, S. H. *et al.* Bulk heterojunction solar cells with internal quantum efficiency approaching 100%. *Nature Photon.* **3,** 297–303 (2009).
5. Margapoti, E. *et al.* Excimer emission in single layer electroluminescent device based on [Ir(4, 5-diphenyl-2-methylthiazolo)$_2$ (5-methyl-1, 10-phenanthroline)]$^+$[PF$_6$]$^-$. *J. Phys. Chem. C* **113,** 12517–12522 (2009).
6. Chua, L-L. *et al.* General observation of n-type field-effect behaviour in organic semiconductors. *Nature* **434,** 194–199 (2005).
7. Muccini, M. A bright future for organic field-effect transistors. *Nature Mater.* **5,** 605–613 (2006).
8. Hepp, A. *et al.* Light-emitting field-effect transistor based on tatracene thin film. *Phys. Rev. Lett.* **91,** 157406 (2003).
9. Rost, C. *et al.* Ambipolar light-emitting organic field-effect transistor. *Appl. Phys. Lett.* **85,** 1613–1615 (2004).
10. Takenobu, T. *et al.* High current density in light-emitting transistors of organic single crystals. *Phys. Rev. Lett.* **100,** 066601 (2008).
11. Verlaak, S., Cheyns, D., Debucquoy, M., Arkhipov, V. & Heremans, P. Numerical simulation of tetracene light-emitting transistors: A detailed balance of exciton processes. *Appl. Phys. Lett.* **85,** 2405–2407 (2004).
12. Gehlhaar, R., Yahiro, M. & Adachi, C. Finite difference time domain analysis of the light extraction efficiency in organic light-emitting field-effect transistors. *J. Appl. Phys.* **104,** 331161–331165 (2008).
13. Santato, C. *et al.* Tetracene light-emitting transistors on flexible plastic substrates. *Appl. Phys. Lett.* **86,** 1411061–1411063 (2005).
14. Cicoria, F. *et al.* Organic light-emitting transistors based on solution-cast and vacuum-sublimed films of a rigid core thiophene oligomer. *Adv. Mater.* **18,** 169–174 (2006).
15. Capelli, R. *et al.* Investigation of the opto-electronic properties of organic light emitting transistors based on an intrinsically ambipolar material. *J. Phys. Chem. C* **112,** 12993–12999 (2008).
16. Yuen, M-Y. *et al.* Semiconducting and electroluminescent nanowires self-assembled from organoplatinum(II) complexes. *Angew. Chem. Int. Ed.* **47,** 9895–9899 (2008).
17. Yamamoto, H., Oyamada, T., Sasabe, H. & Adachi, C. Amplified spontaneous emission under optical pumping from an organic semiconductor laser structure equipped with transparent carrier injection electrodes. *Appl. Phys. Lett.* **84,** 1401–1403 (2004).
18. Baldo, M. A., Holmes, R. J. & Forrest, S. R. Prospects for electrically pumped organic lasers. *Phys. Rev. B* **66,** 035321 (2002).
19. List, E. J. W. *et al.* Interaction of singlet excitons with polarons in wide band-gap organic semiconductors: A quantitative study. *Phys. Rev. B* **64,** 155204 (2001).
20. Staudigel, J., Stößel, M., Steuber, F. & Simmerer, J. A quantitative numerical model of multilayer vapor-deposited organic emitting diodes. *J. Appl. Phys.* **86,** 3895–3910 (1999).
21. Gärtner, C., Karnutsch, C. & Lemmer, U. The influence of annihilation processes on the threshold current density of organic laser diodes. *J. Appl. Phys.* **101,** 231071–231079 (2007).
22. Swensen, J. S., Soci, C. & Heeger, A. J. Light emission from an ambipolar semiconducting polymer field-effect transistor. *Appl. Phys. Lett.* **87,** 253511 (2005).
23. Zaumseil, J., Friend, R. H. & Sirringhaus, H. Spatial control of the recombination zone in an ambipolar light-emitting organic transistor. *Nature Mater.* **5,** 69–74 (2006).
24. Zaumseil, J., Donley, C. L., Kim, J-S., Friend, R. H. & Sirringhaus, H. Efficient top-gate, ambipolar, light-emitting field-effect transistors based on a green-light-emitting polyfluorene. *Adv. Mater.* **18,** 2708–2712 (2006).
25. Bisri, S. Z. *et al.* High mobility and luminescent efficiency in organic single-crystal light-emitting transistors. *Adv. Funct. Mater.* **19,** 1728–1735 (2009).
26. Wang, Y., Kumashiro, R., Nouchi, R., Komatsu, N. & Tanigaki, K. Influence of interface modifications on carrier mobilities in rubrene single crystal ambipolar field-effect transistors. *J. Appl. Phys.* **105,** 124912 (2009).
27. Schidleja, M., Melzer, C. & Seggern, H. Electroluminescence from a pentacene based ambipolar organic field-effect transistor. *Appl. Phys. Lett.* **94,** 123307 (2009).
28. Zaumseil, J. *et al.* Quantum efficiency of ambipolar light-emitting polymer field-effect transistors. *J. Appl. Phys* **103,** 064517 (2008).
29. Ke, T-H. *et al.* High efficiency blue light emitting unipolar transistor incorporating multifunctional electrodes. *Appl. Phys. Lett.* **94,** 1533071–1533073 (2009).
30. Namdas, E. B. *et al.* Gate-controlled light emitting diodes. *Adv. Mater.* **20,** 1321–1324 (2008).
31. Suganuma, N., Shimoji, N., Oku, Y. & Matsushige, K. Novel organic light-emitting transistors with PN-heteroboundary carrier recombination sites fabricated by lift-off patterning of organic semiconductor thin-films. *J. Mater. Res.* **22,** 2982–2986 (2007).
32. Namdas, E. B., Ledochowitsch, P., Yuen, J. D., Moses, D. & Heeger, A. J. High performance light emitting transistors. *Appl. Phys. Lett.* **92,** 183304 (2008).
33. Dinelli, F. *et al.* High-mobility ambipolar transport in organic light-emitting transistors. *Adv. Mater.* **18,** 1416–1420 (2006).
34. Matsushima, T. & Adachi, C. Extremely low voltage light-emitting diodes with p-doped alpha-sexithiophene hole transport and n-doped phenyldipyrenylphosphine oxide electron transport layers. *Appl. Phys. Lett.* **89,** 253506 (2006).

35. Facchetti, A. *et al.* Building blocks for n-type molecular and polymeric electronics. perfluoroalkyl- versus alkyl-functionalized oligothiophenes (*nT*; *n* = 2–6). Systematics of thin film microstructure, semiconductor performance, and modeling of majority charge injection in field-effect transistors. *J. Am. Chem. Soc.* **126**, 13859–13874 (2004).

36. Garnier, F. *et al.* Dihexylquaterthiophene, a two-dimensional liquid crystal-like orgnic semiconductor with high transport properties. *Chem. Mater.* **10**, 3334–3339 (1998).

37. Schols, S. *et al.* Organic light-emitting diodes with field-effect-assisted electron transport based on α,ω-diperfluorohexyl-quaterthiophene. *Adv. Funct. Mater.* **18**, 3645–3652 (2008).

38. Ackermann, J. *et al.* Control of growth and charge transport properties of quaterthiophene thin films via hexyl chain substitutions. *Org. Electr.* **5**, 213–222 (2004).

39. Loi, M. A. *et al.* Supramolecular organization in ultra-thin films of α-sexithiophene on silicon dioxide. *Nature Mater.* **4**, 81–85 (2005).

40. Da Como, E., Loi, M. A., Murgia, M., Zamboni, R. & Muccini, M. J-aggregation in α-sexithiophene submonolayer films on silicon dioxide. *J. Am. Chem. Soc.* **128**, 4277–4281 (2006).

41. Yan, H., Kagata, T. & Okuzaki, H. Ambipolar pentacene/C60-based field-effect transistors with high hole and electron mobilities in ambient atmosphere. *Appl. Phys. Lett.* **94**, 023305 (2009).

42. Ye, R., Baba, M., Ohta, K., Kazunori Suzuki, K. & Mori, K. Fabrication of ambipolar organic heterojunction transistors with various sexithiophene alkyl-substituted derivatives. *Jpn. J. Appl. Phys.* **48**, 04C168 (2009).

43. Li, J-F., Chang, W-L., Ou, G-P. & Zhang, F-J. Air-stable ambipolar organic field effect transistors with heterojunction of pentacene and *N,N'*-bis(4-trifluoromethylben-zyl) perylene-3,4,9,10- tetracarboxylic diimide. *Chin. Phys. B* **18**, 3002–3007 (2009).

44. Uddin, A., Lee, C. B., Hu, X., Wong, T. K. S. & Sun, X. W. Effect of doping on optical and transport properties of charge carries in Alq₃. *J. Cryst. Growth* **288**, 115–118 (2006).

45. Muck, T. *et al. In situ* electrical characterization of DH4T field-effect transistors. *Synth. Met.* **146**, 317–320 (2004).

46. DiBenedetto, S. A., Facchetti, A., Rainer, M. A. & Marks, T. J. Molecular self-assembled monolayers and multilayers for organic and unconventional inorganic thin-film transistor applications. *Adv. Mater.* **21**, 1407–1433 (2009).

47. Pinto, J. C. *et al.* Organic thin film transistors with polymer brush gate dielectrics synthesized by atom transfer radical polymerization. *Adv. Funct. Mater.* **18**, 36–43 (2008).

Acknowledgements

Author contributions

R.C. defined the concept of the trilayer heterostructure, fabricated devices, executed optoelectronic experiments, analysed and interpreted results. S.T. defined the concept of the trilayer heterostructure, executed spectroscopic and photonic experiments, analysed and interpreted results. G.G. carried out AFM measurements, contributed to fabricate devices and to execute optoelectronic experiments. H.U. synthesized DH-4T and DFH-4T. A.F. supervised the synthesis and discussed the results. M.M. defined the concept of the trilayer heterostructure, took part to the key experiments, interpreted results and supervised the entire work. A.F. and M.M. wrote the manuscript.

Additional information

The authors declare no competing financial interests. Supplementary information accompanies this paper on www.nature.com/naturematerials. Reprints and permissions information is available online at http://npg.nature.com/reprintsandpermissions. Correspondence and requests for materials should be addressed to R.C. or M.M.